Noname manuscript No.
(will be inserted by the editor)

An Analytic Solution to the Coupled Pressure-Temperature Equations for Modeling of Photoacoustic Trace Gas Sensors

Jordan Kaderli · John Zweck · Artur Safin · Susan E. Minkoff

the date of receipt and acceptance should be inserted later

Abstract Trace gas sensors have a wide range of applications including air quality monitoring, industrial process control, and medical diagnosis via breath biomarkers. Quartz-enhanced photoacoustic spectroscopy and resonant optothermoacoustic detection are two techniques with several promising advantages. Both methods use a quartz tuning fork and modulated laser source to detect trace gases. To date, these complementary methods have been modeled independently and have not accounted for the damping of the tuning fork in a principled manner. In this paper we discuss a coupled system of equations derived by Morse and Ingard for the pressure, temperature, and velocity of a fluid that accounts for both thermal effects and viscous damping, and which can be used to model both types of trace gas sensors simultaneously. As a first step towards the development of a more realistic model of these trace gas sensors, we derive an analytical solution to a pressure-temperature subsystem of the Morse-Ingard equations in the special case of cylindrical symmetry. We solve for the pressure and temperature in an infinitely long cylindrical fluid domain with a source function given by a constant-width Gaussian beam that is aligned with the axis of the cylinder. In addition, we surround this cylinder with an infinitely long annular solid domain, and we couple the pressure and temperature in the fluid domain to the temperature in the solid. We show that the temperature in the solid near the fluid-solid interface can be at least an order of magnitude larger than that computed using a simpler model in which the temperature in the fluid is governed by the heat equation rather than by the Morse-Ingard equations. In addition, we verify that the temperature solution of the coupled system exhibits a thermal boundary layer. These results strongly suggest that for computational modeling of resonant optothermoacoustic detection sensors, the temperature in the fluid should be computed by solving the Morse-Ingard equations rather than the heat equation.

Keywords trace gas sensing · optothermal detection · mathematical modeling · photoacoustic spectroscopy · viscothermal effects

1 Introduction.

Many applications in science and engineering, such as the design of trace gas sensors, hearing aid transducers, and micro-electrical-mechanical devices, involve the interaction between a pressure wave and a thermal wave on a very small scale [8,17]. Models that use either the acoustic wave equation or the heat equation do not account for viscothermal effects [8]. Instead, by using a set of coupled equations involving pressure, temperature and fluid velocity that are derived from the Navier-Stokes equations, one can examine thermal and viscous boundary layer phenomena and more accurately calculate resonances [15,16]. In a study of reduced models for thermal phenomena near thin bodies in a fluid, Lavergne *et al.* [22] showed that thermal boundary layer effects can be significantly different for planar membranes than for cylindrical fibers. In their modeling of hearing aid receivers, Cordioli *et al.* [8] show that experimentally measured resonance frequency curves agree much better with results obtained from models that incorporate viscothermal effects than with models based on the acoustic wave equation.

Analytical solutions to the coupled pressure-temperature-velocity system have been derived by several authors for a variety of applications, and used to determine the limitations of the

Department of Mathematical Sciences, The University of Texas at Dallas, 800 West Campbell Road, Richardson, TX 75080-3021
E-mail: jxk124230@utdallas.edu, zweck@utdallas.edu, aks084000@utdallas.edu, sminkoff@utdallas.edu

acoustic wave equation at small scales where viscous and thermal effects may be significant. For example, Morse and Ingard [29] derived plane wave solutions both in free space and near a planar boundary, and used them to determine the width of viscous and thermal boundary layers. Joly *et al.* [16] studied admittance properties for the reflection of a pressure wave incident on a rigid wall, accounting for viscous and thermal effects in the fluid and thermal diffusion into the wall. For their study of photoacoustic effects in small droplets, Cao and Diebold [6] derived a spherically symmetric solution of a coupled system for pressure and temperature with a spatially uniform heat source, and applied the solution to study the limitations of the acoustic wave equation when the radii of the droplets approaches the characteristic lengths for fluid viscosity and thermal conduction.

In this paper, we derive an analytical solution to a coupled system of equations derived by Morse and Ingard for the pressure and temperature variations in a fluid due to a heat source that is internal to the fluid. We use this solution to study how the interaction between the pressure and temperature near a fluid-solid interface gives rise to a thermal boundary layer that affects the diffusion of heat into the solid. Our motivation for studying this problem is to investigate whether the coupled equations for pressure, temperature, and fluid velocity can be used to improve computational models of a class of trace gas sensors that employ a quartz tuning fork to detect the weak acoustic pressure waves and thermal disturbances that are generated when a trace gas is heated by a laser [19,20]. The results we will present in this paper demonstrate that for the modeling of a trace gas sensor designed to detect thermal disturbances, it is necessary to solve the coupled pressure-temperature system rather than simply relying on the heat equation in the fluid, as was done in previous modeling work [36].

Trace gas sensors are currently being developed for a diverse range of applications including air quality monitoring, industrial process control, medical diagnosis via breath analysis, and explosives detection [9,23,38]. An important class of trace gas sensors are photoacoustic spectroscopy (PAS) sensors which detect the weak acoustic pressure waves that are generated when optical radiation from a laser is periodically absorbed by molecules of a trace gas [2,27]. A PAS sensor that has garnered much recent attention is the quartz-enhanced photoacoustic spectroscopy (QEPAS) sensor, which employs a quartz tuning fork to detect these acoustic pressure waves via the piezoelectric effect [19,33].

In addition to generating an acoustic pressure wave, the periodic interaction between the laser radiation and a trace gas also generates a thermal diffusion wave in the fluid. The same tuning fork can be used to detect this thermal diffusion wave via the indirect pyroelectric effect [20,31]. This trace gas sensing modality is referred to as Resonant OptoThermoAcoustic DEtection (ROTADE). Because the thermal diffusion wave attenuates very rapidly, in most operating regimes the acoustic wave has a much greater effect on the tuning fork than does the thermal wave. However, when the ambient pressure is sufficiently low and the laser source is positioned close enough to the surface of the tuning fork, the thermal wave can dominate [20, 36]. Since the lines in the absorption spectrum become more distinct as the ambient pressure is lowered, ROTADE sensors provide more wavelength selectivity than do QEPAS sensors, which is important for some applications.

QEPAS and ROTADE sensor technologies are based on the following physical processes. A laser generates optical radiation at a specific absorption wavelength of the trace gas to be detected. The optical energy absorbed by the trace gas is transformed into vibrational energy of the gas molecules. By sinusoidally modulating the interaction between the laser radiation and the trace gas, a thermal diffusion wave is generated in the ambient fluid. In addition, vibrational-to-translational energy conversion processes at the molecular level generate an acoustic pressure wave. In a QEPAS sensor, the acoustic pressure wave induces a mechanical vibration of the tuning fork, which is in turn converted to an electric current via the piezoelectric effect in quartz. QEPAS systems are highly sensitive trace gas sensors which can detect minute amounts of trace gas at the parts-per-billion level [25,39]. This sensitivity is achieved by directing the laser beam between the tines of the tuning fork (see Figure 1, left) and choosing the laser modulation frequency to excite a strong resonance in the tuning fork. Since the entire process is linear, the amplitude of the received electrical signal is proportional to the concentration of the trace gas. In those operating regimes for which the thermal diffusion wave dominates over the acoustic pressure wave on the surfaces of the tuning fork, the device acts as a ROTADE sensor. When the excited molecules collide with the surface of the tuning fork, their vibrational energy is transferred to the tuning fork in the form of heat. The thermal energy transferred to

the surface then diffuses into the interior of the tuning fork where it induces a mechanical stress and displacement of the tines of the tuning fork. In summary, the ROTADE sensor utilizes a combination of the thermoelastic effect, in which heat generates mechanical stress, and the piezoelectric effect, in which this stress generates an electrical signal. The combination of these two effects is called the indirect pyroelectric effect [31].

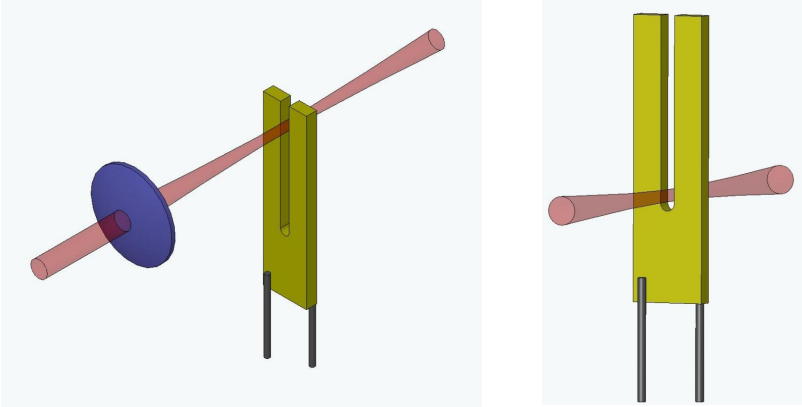

Fig. 1 Schematic diagram of a QEPAS sensor (left) and a ROTADE sensor (right). Each figure shows the quartz tuning fork (mustard) and laser source (pink).

At low ambient pressure, the same tuning fork can act as both a QEPAS sensor and a ROTADE sensor. In this situation the placement of the laser beam relative to the tuning fork dictates which sensing modality is dominant. When the laser is directed near the top of the tines of the tuning fork the QEPAS signal is dominant (see Figure 1, left), whereas when the laser beam is directed near the base of the tuning fork the ROTADE signal is dominant (see Figure 1, right). Laboratory experiments suggest that as the laser source is moved down from the top of the tuning fork to its base, at some point the QEPAS and ROTADE signals destructively interfere with one another [20,36].

QEPAS and ROTADE sensors have several promising advantages over traditional trace gas sensors, including their small size (1000 times smaller than traditional sensors), immunity to environmental noise, and improved sensitivity [20,23,38]. The high degree of sensitivity of QEPAS and ROTADE sensors is primarily due to the very strong resonances of tuning fork oscillators. In general for an oscillator, smaller damping effects result in larger resonance amplitudes and narrower resonance frequency widths. Physically realistic modeling of damping is therefore critical for accurate computational modeling of QEPAS and ROTADE sensors [12]. In particular, since the overall damping effect depends on the geometric configuration of the system, such models need to allow for the geometry of the tuning fork to be varied. Firebaugh *et al.* [12, 13] obtained reasonable agreement between a computational model and experimental data in a study comparing the performance characteristics of several different tuning fork geometries for a QEPAS sensor. Previous work with a simplified model of a ROTADE sensor by Petra *et al.* [36] demonstrated that computer simulations can be used to optimize the tuning fork geometry in an efficient manner. However, *ad-hoc* damping models were used in all these studies. For example, Petra *et al.* [35,36] incorporated an *ad-hoc* damping term into the equations describing the resonant vibration of the tuning fork, in which the damping constant was fitted to experimentally measured data from a single tuning fork.

The major source of damping in tuning fork oscillators is viscous damping due to the motion of the oscillator through the ambient fluid [30]. Kokubun *et al.* [18] developed a theoretical model of the viscous damping of a tuning fork in which the drag force is calculated using fluid mechanics. By approximating a tuning fork by a string of spherical beads, they were able to apply an analytical formula for the drag force on a sphere [21] to approximate the drag force on a vibrating tuning fork.[1] However, because of its *ad-hoc* nature, Kokubun *et al.* used a curve fitting algorithm to determine the radius of the sphere in the model using data obtained from experimental measurements of specific tuning forks. Firebaugh *et al.* [12,13] obtained

[1] These formulae were obtained by solving the incompressible linear Navier-Stokes equation for viscous fluid flow around a sphere.

qualitative—though not quantitative—agreement with experiments using a finite-element model of a QEPAS sensor that incorporated viscous damping of the tuning fork using the approach of Kokubun *et al.* They attributed the lack of quantitative agreement to the oscillating sphere approximation used to model the viscous damping of the tuning fork.

In this paper, we take the first step towards the development of a joint mathematical model for QEPAS and ROTADE phenomena that more accurately incorporates viscous damping and thermal conduction effects. This new model will in the future allow for numerical optimization of the geometric parameters of the tuning fork in these sensors. Viscous and thermal effects in an acoustic fluid play a significant role only near the boundaries of the fluid. For harmonic plane waves, the thickness of the viscous and thermal boundary layers are each on the order of 10 μm at the 32.8 kHz operating frequency of the sensor [29]. By comparison, depending on the design of the system, the smallest characteristic length of the geometric domain ranges from 30-100 μm [10]. Because the thickness of the boundary layers is within an order of magnitude of the smallest characteristic length of the geometric domain, rather than treating the boundary layer separately [3], we instead use a modification of the classical equations for acoustic pressure and heat conduction in the entire fluid domain that correctly accounts for thermal and viscous effects. This modification was obtained by Morse and Ingard [29], who linearized the Navier Stokes equations to derive a coupled system of linear partial differential equations for the acoustic pressure, temperature, and fluid velocity that includes the effects of fluid viscosity and thermal conduction. By decoupling the equations for the fluid velocity from those for the other two variables, they obtained a pair of equations for the pressure and temperature. The pressure and temperature equations are coupled to each other through a term that involves the viscosity and thermal conduction parameters of the fluid. In this paper, we add a source term to the temperature equation which enables us to model the generation of the thermal diffusion wave and its conversion to an acoustic pressure wave in photoacoustic spectroscopy and resonant optothermoacoustic trace gas sensors [28].

As a first step towards our goal of developing a realistic model of the coupled thermal and pressure waves, in this paper we derive an analytical solution to the Morse-Ingard equations for pressure and temperature in the special case of cylindrical symmetry. Specifically, the simplified situation we consider is to solve the Morse-Ingard equations in an infinitely long cylindrical fluid domain with a source function given by a constant-width Gaussian beam that is aligned with the axis of the cylinder. Furthermore, we surround this cylinder with an infinitely long annular solid domain, and we couple the pressure and temperature in the fluid domain to the temperature in the solid, which we model using the heat equation. Because of the symmetries inherent in this simplified problem, the solutions of the coupled system are functions only of the radial distance from the axis of the cylinder. In particular, the analytical solution we derive does not capture any variations of pressure and temperature along the axis of the cylinder. We will use the resulting solution to gain insight into how the thermal boundary layer in the fluid affects the temperature variation *in the solid* near the fluid-solid interface. We show that both the pressure and temperature variations in the fluid are the sum of a small scale thermal mode and a large scale acoustic mode. For the pressure, we show that the acoustic mode dominates over the thermal mode. However, we will show that the temperature in the solid near the fluid-solid interface can be at least an order of magnitude larger than that computed using a simpler model in which the temperature in the fluid is governed by the heat equation rather than by the Morse-Ingard equations.

Globally, the geometry of a tuning fork is very different from the geometry of an infinitely long annular domain. However, experiments and simulations have shown that the performance of a ROTADE sensor is to a large extent determined by the temperature in that region of the tuning fork that is closest to the laser beam [34,36]. Moreover, in a ROTADE sensor, the laser beam is positioned close to the U-shaped surface near the base of the tines of the tuning fork, and this surface is locally well approximated by the boundary of a half-cylinder (see Figure 1, right). In laboratory experiments of ROTADE sensors, the acoustic pressure of the fluid is not resonant. Rather, the frequency of the source is chosen to excite a mechanical resonance in the tuning fork. Similarly, although the cylindrical fluid domain of the simplified system is enclosed by the solid, the frequency of the source does not excite an acoustical resonance in the radial direction. Nevertheless, since the pressure variation decays slowly it depends on the global geometry of the system. In summary, although the global geometry of the simplified system is different from that of a trace gas sensor system, the local similarities between the two systems

are strong enough that our conclusions about the temperature in the solid should carry over to ROTADE sensors. In particular, our results strongly indicate the necessity of modeling the temperature in the fluid using the Morse-Ingard equations, rather than using the heat equation. Indeed, in our previous modeling of ROTADE sensors that was based on the heat equation in the fluid, we could only obtain agreement between normalized signal amplitudes rather than between the amplitudes themselves [36]. While there are several factors that could contribute to this lack of agreement, the discrepancy between the results obtained using the Morse-Ingard equation and the heat equation in the fluid is likely one of them.

In Section 2 we briefly review the derivation of the Morse-Ingard equations. In Section 3 we derive an analytic solution of these equations. In Section 4 we describe the finite-element computation we performed to verify the correctness of the analytic solution. In Section 5 we present the results we obtained using both the analytical solution and finite-element method. Finally, in Section 6 we summarize the results and discuss future work.

2 Model.

In previous work, Petra *et al.* [34–37] developed separate models for QEPAS and ROTADE sensors. In the case of a QEPAS sensor, in which a pressure wave generates the electrical signal, Petra *et al.* used the acoustic wave equation to model wave propagation [35]. Similarly, in the case of a ROTADE sensor, in which periodic thermal expansion generates the electrical signal, they used the heat equation to describe the diffusion of the gas [36]. In this paper, we simultaneously model the temperature and pressure in an acoustic fluid using a coupled system of equations derived by Morse and Ingard [29, p. 279-282]. These equations are obtained from a system of equations for pressure, temperature, and fluid velocity that was independently obtained by Morse and Ingard [29], Miklos, Shäfer and Hess [28], and Joly *et al.* [16].

We consider a fluid that in the absence of a heat source has uniform density, pressure, and temperature, and is everywhere at rest. When heat energy is introduced into the fluid, for example by the interaction between a laser and a trace gas, the thermodynamic quantities vary from their ambient values. To derive equations for the variation of pressure, temperature, and velocity we begin by considering the linearized Navier-Stokes equations,

$$\rho_0 \frac{\partial \mathbf{v}}{\partial t} = -\nabla \mathcal{P} + \left(\eta + \frac{1}{3}\mu\right) \nabla \left(\nabla \cdot \mathbf{v}\right) + \mu \nabla \left(\nabla \cdot \mathbf{v}\right) - \mu \left(\nabla \times \left(\nabla \times \mathbf{v}\right)\right), \tag{1}$$

where $\mathbf{v}$ is the fluid velocity, ρ_0 is ambient density, t is time, $\mathcal{P}$ is the variation from the ambient pressure, and μ and η are the viscosity and bulk viscosity of the fluid, respectively. By the Helmholtz Decomposition Theorem, we can express the fluid velocity in the form $\mathbf{v} = \mathbf{v}_\ell + \mathbf{v}_t$ where the lamellar part, $\mathbf{v}_\ell$, is curl free and the rotational part, $\mathbf{v}_t$, is divergence free.[2] Because $\nabla \mathcal{P}$ is also curl free, we can use this decomposition to obtain separate equations for the lamellar and rotational parts:

$$\rho_0 \frac{\partial \mathbf{v}_\ell}{\partial t} = -\nabla \mathcal{P} + \left(\eta + \frac{4}{3}\mu\right) \nabla \left(\nabla \cdot \mathbf{v}_\ell\right), \tag{2}$$

$$\rho_0 \frac{\partial \mathbf{v}_t}{\partial t} = -\mu \left(\nabla \times \left(\nabla \times \mathbf{v}_t\right)\right). \tag{3}$$

In addition to the Navier-Stokes equations, we consider the continuity of mass flow equation,

$$\frac{\partial \rho}{\partial t} + \rho_0 \nabla \cdot \mathbf{v} = 0, \tag{4}$$

where ρ is the variation of the ambient density, ρ_0, and the continuity of heat flow equation,

$$\mathcal{T}_0 \frac{\partial \zeta}{\partial t} = K \nabla^2 \mathcal{T}, \tag{5}$$

[2] A theorem in the text of Chorin and Marsden [7] states that for a vector field, $\mathbf{v}$, on a domain $\Omega \subset \mathbb{R}^3$, the Helmholtz decomposition, $\mathbf{v} = \mathbf{v}_\ell + \mathbf{v}_t$, is unique, provided that we also assume that $\mathbf{v}_t$ is tangential to the boundary surface, $\partial\Omega$.

where $\mathcal{T}$ is the variation from the ambient temperature, $\mathcal{T}_0$, ζ is the variation of the entropy, and K is the thermal conductivity. We also consider the equation of state,

$$\rho = \gamma\rho_0\kappa_S\left(\mathcal{P} - \alpha\mathcal{T}\right), \tag{6}$$

where γ is the ratio of specific heats and κ_S is the adiabatic compressibility. In addition, the parameter, α, is given by $\alpha = \rho_0\beta c^2/\gamma$, where c is the speed of sound and β is the coefficient of thermal expansion of the fluid. Finally, the equation for the variation of the entropy is given by

$$\zeta = \frac{C_p}{\mathcal{T}_0}\left(\mathcal{T} - \frac{\gamma-1}{\alpha\gamma}\mathcal{P}\right), \tag{7}$$

where C_p is the specific isobaric heat capacity of the fluid. Equations (2)–(7) form a system of six equations for the fluid velocity and the variations in the pressure, temperature, density, and entropy. Eliminating ζ and ρ from Equations (4)–(7) and focusing on the temperature variation, $\mathcal{T}$, and pressure variation, $\mathcal{P}$, of the fluid, we obtain:

$$\frac{\partial}{\partial t}\left(\mathcal{T} - \frac{\gamma-1}{\gamma\alpha}\mathcal{P}\right) - l_h c\nabla^2\mathcal{T} = \mathcal{S}, \tag{8}$$

$$\frac{\gamma}{c^2}\left(\frac{\partial^2}{\partial t^2} - l_v c\frac{\partial}{\partial t}\nabla^2\right)\left(\mathcal{P} - \alpha\mathcal{T}\right) - \nabla^2\mathcal{P} = 0, \tag{9}$$

$$\rho_0\frac{\partial \mathbf{v}_\ell}{\partial t} = -\nabla\left[\mathcal{P} + \frac{\gamma l_v}{c}\frac{\partial}{\partial t}\left(\mathcal{P} - \alpha\mathcal{T}\right)\right], \tag{10}$$

where $\mathcal{S} = \mathcal{S}(\mathbf{x}, t)$ is the amount of heat per unit time provided by the source, t is time, and $\mathbf{x}$ is position. We added the source term, $\mathcal{S}$, to Equation (8) to model the heating of the fluid by the laser [16,28]. The parameter $l_v = \left(\frac{4}{3} + \frac{\eta}{\mu}\right)\frac{\mu}{\rho_0 c}$ is the viscous characteristic length, and $l_h = K/\rho_0 c C_p$ is the thermal characteristic length. We refer to Equations (3) and (8)–(10) as the Morse-Ingard equations. Equations (8) and (9), which are independent of the fluid velocity, $\mathbf{v}$, can be solved as a system of two equations to determine the temperature and pressure variations. In this paper we focus on Equations (8) and (9), since the tuning fork in a trace gas sensor is designed to detect the pressure and temperature variations. For a tuning fork sensor, it is only necessary to solve for the fluid velocity in situations where the damping of the tuning fork cannot be obtained from experimental measurements. However, in future computational models we will also include Equations (3) and (10) for the fluid velocity. The fluid velocity is needed to impose the conditions at the interface between the fluid and tuning fork that are required to compute the effect of the viscous damping of the tuning fork by the fluid.

Since the tuning forks used in QEPAS and ROTADE sensors are sharply resonant, it is reasonable to assume that the source, $\mathcal{S}$, is harmonic in time [35]. Consequently, we model the source as an axially symmetric Gaussian beam of width σ of the form

$$S(r,t) = \Re\left\{C\exp\left[-r^2/\left(2\sigma^2\right)\right]\exp(-i\omega t)\right\}, \tag{11}$$

where r is radial distance from the axis of the laser beam and $\Re(z)$ denotes the real part of a complex number, z. The angular frequency, ω, is given by $\omega = 2\pi f$, where f is the wave frequency. This frequency is chosen to match the resonance frequency of the tuning fork, which is typically $f = 32.8$ kHz. The parameter, C, is given by $C = \alpha_{\text{eff}} W_L/\left(4\pi\rho_0 C_p\sigma^2\right)$ where α_{eff} is the effective absorption coefficient (i.e., the fraction of radiation absorbed per unit length as it passes through fluid), and W_L is the laser power [35].

To enable us to derive cylindrically symmetric solutions, we solve the Morse-Ingard Equations (8) and (9) with a source function given by Equation (11) in an infinitely long cylindrical fluid domain, Ω_{fluid}, of radius, R, that is aligned with the axis of the laser beam. Furthermore, we couple the pressure and temperature variations in the fluid to the temperature variation in an infinitely long annular solid domain, Ω_{solid}, surrounding the fluid with inner radius, R, and outer radius, R_S. We show a cross section of the composite domain, $\Omega = \Omega_{\text{fluid}} \cup \Omega_{\text{solid}}$ in Figure 2.

We will use the resulting analytical solution to gain insight into how the thermal boundary layer in the fluid affects the temperature variation in the solid near the fluid-solid interface.

We anticipate that the behavior of the temperature variation in the solid near the fluid-solid interface obtained on the simplified geometric domain will be similar to that in the tuning fork of a ROTADE sensor. In particular, experiments have shown that that the performance of a ROTADE sensor is to a large extent determined by the temperature in that region of the tuning fork that is closest to the laser beam [34,36]. Moreover, since the laser beam is positioned close to the U-shaped surface near the base of the tuning fork, locally in this region, the boundary is well approximated by the boundary of a half-cylinder (see Figure 1, right).

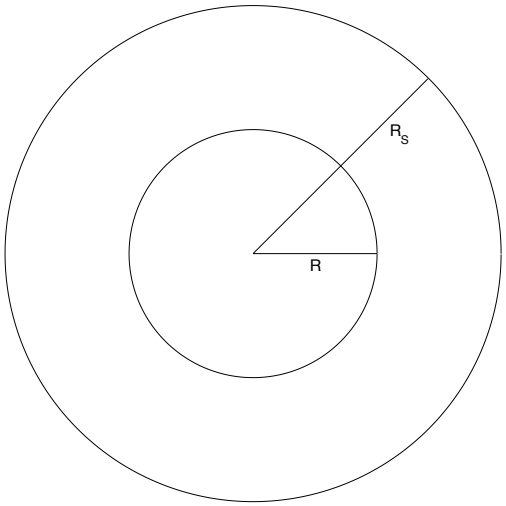

Fig. 2 Cross section of a cylindrical fluid domain of radius, R, surrounded by an annular solid domain with outer radius, R_S.

Because of the cylindrical symmetry of the both source function, S, and the composite domain, $\Omega = \Omega_{\text{fluid}} \cup \Omega_{\text{solid}}$, the temperature and pressure variations are functions only of the radial distance, r, from the axis of the laser beam. Moreover, since we are only interested in time-harmonic, steady-state solutions, we can express the pressure, temperature, and source in the form

$$\mathcal{P}(r,t) = \Re\left\{P(r)\, e^{-i\omega t}\right\}, \qquad \mathcal{T}(r,t) = \Re\left\{T(r)\, e^{-i\omega t}\right\}, \qquad \mathcal{S}(r,t) = \Re\left\{S(r)\, e^{-i\omega t}\right\}. \quad (12)$$

Under these assumptions, the coupled system of time-dependent partial differential equations (8) and (9) reduces to the coupled Helmholtz system of second-order ordinary differential equations,

$$l_h c\nabla^2 T + i\omega\left(T - \frac{\gamma-1}{\gamma\alpha}P\right) = -S, \quad (13)$$

$$\nabla^2 P + \frac{\gamma}{c^2}\left(\omega^2 - i l_v c\omega\nabla^2\right)(P - \alpha T) = 0, \quad (14)$$

where the Laplacian operator of a function, $F = F(r)$, is given by $\nabla^2 F = F'' + \frac{1}{r}F'$. Here $F' = dF/dr$.

The temperature, $\mathcal{T}_S$, in the solid, Ω_{solid}, satisfies the heat equation

$$\frac{\partial \mathcal{T}_S}{\partial t} - D_S\nabla^2\mathcal{T}_S = 0, \quad (15)$$

where D_S is the thermal diffusivity of the solid. Assuming a time-harmonic solution, we have that $\mathcal{T}_S(r,t) = \Re\{T_S(r)\, e^{-i\omega t}\}$ and so the Helmholtz form of Equation (15) is

$$T_S'' + \frac{1}{r}T_S' + \frac{i\omega}{D_S}T_S = 0, \quad (16)$$

which has the solution

$$T_S(r) = d_1 J_0(kr) + d_2 H_0^{(1)}(kr). \quad (17)$$

Here $k = \sqrt{\frac{i\omega}{D_S}}$ and J_0 is the zeroth order Bessel function of the first kind and $H_0^{(1)}$ is the zeroth order Hankel function of the first kind [32]. We express the solution using this particular linear combination because J_0 and $H_0^{(1)}$ form a numerically satisfactory pair of cylinder functions in the upper half of the complex plane [32, 10.2(iii)].

In Section 3, we will derive a formula for the general solution of Equations (13) and (14) in terms of Bessel and Hankel functions. Because these equations are both of second order, the general solution will have four unknown constants. In addition, the temperature solution in the annulus given by Equation (17) has two unknown constants, d_1 and d_2. To determine these six constants we impose the six conditions,

$$T(0) < \infty, \tag{18}$$
$$P(0) < \infty, \tag{19}$$
$$T(R) = T_S(R), \tag{20}$$
$$K_F \nabla T(R) = K_S \nabla T_S(R), \tag{21}$$
$$P'(R) = 0, \tag{22}$$
$$T_S(R_S) = 0, \tag{23}$$

where K_F and K_S are the thermal conductivities of the fluid and solid, respectively. The first two conditions are necessary to guarantee that the solution is bounded, since the Hankel functions have a singularity at zero. The third and fourth conditions ensure continuity of temperature and heat flux across the fluid-solid interface. The fifth condition ensures that the normal derivative of the pressure is zero at the fluid-solid interface. To a first approximation, this assumption is reasonable when modeling the acoustic pressure in a trace gas sensor that employs a tuning fork, since the amplitude of vibration of the tuning fork is several orders of magnitude smaller than the characteristic lengths of the system. Therefore, it is reasonable to also assume that the surface of the annular solid in our simplified model is rigid. The sixth condition states that the temperature variation is zero on the outer wall of the annulus. This assumption is reasonable since the temperature variation is known to decay exponentially in the solid, and because we are most interested in computing the temperature near the inner wall of the annulus.

Imposing the condition $T(R) = 0$ in place of conditions (20), (21), and (23) yields essentially the same solution in the fluid. However, in future work, we will develop a model for a trace gas sensor in which the pressure and temperature in the fluid and the temperature in the tuning fork are coupled to the mechanical deformation of the tuning fork. For this model, setting the temperature to zero on the boundary of the tuning fork would be incorrect as laboratory data has shown that at low ambient pressure the output of the sensor depends on both the pressure variation at the interface and the temperature variation in the tuning fork near the interface. One of our goals in this paper is to determine whether it is necessary to use the coupled system given by Equations (13) and (14) to model the pressure and temperature in the fluid, or whether it is sufficient to separately compute solutions of the acoustic wave and heat equations. Since this question cannot be answered by imposing the condition $T(R) = 0$, we instead use the more realistic conditions (20), (21), and (23).

3 Derivation of the Analytic Solution.

To solve Equations (13) and (14), we adapt the method used by Petra *et al.* [35] who employed the acoustic wave equation to model the propagation of pressure waves in a QEPAS sensor. By considering the Helmholtz form of the equation Petra and coauthors were able to use the method of variation of parameters to derive an analytic solution to the acoustic wave equation in terms of Bessel and Hankel functions. In this section, we use a similar approach to solve the Morse-Ingard equations.

To facilitate the derivation of the solution and to focus attention on the parameters of interest, we nondimensionalize the Morse-Ingard equations using the nondimensional quantities

$$\mathbf{x}_* = \frac{\omega \mathbf{x}}{c}, \quad \nabla_* = \frac{c}{\omega}\nabla, \quad P_* = P\left(\frac{c\mathbf{x}_*}{\omega}\right), \quad T_* = \alpha T\left(\frac{c\mathbf{x}_*}{\omega}\right),$$
$$S_* = -\frac{\alpha}{\omega} S\left(\frac{c\mathbf{x}_*}{\omega}\right), \quad \Omega = \frac{\omega l_h}{c}, \quad \text{and} \quad \Lambda = \frac{\omega l_v}{c}. \tag{24}$$

Substituting these nondimensionalized quantities into Equations (13) and (14) gives

$$\Omega\,\nabla_*^2 T_* + iT_* - i\frac{\gamma-1}{\gamma}P_* \;=\; S_*, \tag{25}$$

$$\nabla_*^2 P_* + \gamma\left(1 - i\Lambda\nabla_*^2\right)\left(P_* - T_*\right) \;=\; 0. \tag{26}$$

To eliminate the spatial derivative of temperature in Equation (26), we substitute Equation (25) into Equation (26) to obtain the new system,

$$\Omega\nabla^2 T + iT - i\frac{\gamma-1}{\gamma}P = S, \tag{27}$$

$$\left(1 - i\gamma\Lambda\right)\nabla^2 P + \left[\gamma\left(1 - \frac{\Lambda}{\Omega}\right) + \frac{\Lambda}{\Omega}\right]P - \gamma\left(1 - \frac{\Lambda}{\Omega}\right)T = -i\gamma\frac{\Lambda}{\Omega}S. \tag{28}$$

Here we have dropped the star notation. However, the reader should keep in mind that we are working with nondimensionalized quantities for the remainder of Section 3. Note that while the equations are still coupled, each has derivatives of temperature or pressure only. Thus we can write Equations (27) and (28) as

$$\Omega\left(T'' + \frac{1}{r}T'\right) + iT - i\frac{\gamma-1}{\gamma}P = S, \tag{29}$$

$$\left(1 - i\gamma\Lambda\right)\left(P'' + \frac{1}{r}P'\right) + \left[\gamma\left(1 - \frac{\Lambda}{\Omega}\right) + \frac{\Lambda}{\Omega}\right]P - \gamma\left(1 - \frac{\Lambda}{\Omega}\right)T = -i\gamma\frac{\Lambda}{\Omega}S. \tag{30}$$

3.1 Solution of the Homogeneous Equations.

We begin by finding the solution of the homogeneous version of the system (29) and (30). When $S = 0$, solving Equation (29) for P gives

$$P = \frac{\gamma}{\gamma-1}\left[T - i\Omega\left(T'' + \frac{1}{r}T'\right)\right]. \tag{31}$$

Because of the presence of the Laplacian in cylindrical coordinates in Equation (31), it is natural to suppose that $T = \mathcal{C}_0\left(kr\right)$, where $\mathcal{C}_0$ is a cylinder function of order zero, i.e., a linear combination of Bessel and Hankel functions of order zero [32], and k is a constant to be determined. Consequently, T satisfies $T'' + \frac{1}{r}T' = -k^2 T$, and so Equation (31) can be rewritten as

$$P = mT = m\mathcal{C}_0\left(kr\right) \quad \text{where} \quad m = \frac{\gamma}{\gamma-1}\left(1 + i\Omega k^2\right). \tag{32}$$

Since P is also a cylinder function, Equation (30) reduces to the algebraic equation

$$\left(1 - i\gamma\Lambda\right)\left(-k^2 P\right) + \left[\gamma\left(1 - \frac{\Lambda}{\Omega}\right) + \frac{\Lambda}{\Omega}\right]P - \gamma\left(1 - \frac{\Lambda}{\Omega}\right)T = 0. \tag{33}$$

Since $P = mT$, and assuming T is not identically zero, we conclude that

$$\left(i\Omega + \gamma\Omega\Lambda\right)k^4 + \left(1 - i\gamma\Omega - i\Lambda\right)k^2 - 1 = 0. \tag{34}$$

Therefore, for $T = \mathcal{C}_0\left(kr\right)$ and $P = m\mathcal{C}_0\left(kr\right)$ to be solutions of the homogeneous equations (29) and (30), the parameter k must be a solution of Equation (34). Consequently,

$$k^2 = \frac{i}{2\Omega}\left(\frac{1 - i\gamma\Omega - i\Lambda \pm Q}{1 - i\gamma\Lambda}\right), \tag{35}$$

where

$$Q^2 = \left(1 - i\gamma\Omega - i\Lambda\right)^2 + 4\left(i\Omega + \gamma\Omega\Lambda\right). \tag{36}$$

Next we define

$$k_t^2 = \frac{i}{2\Omega}\left(\frac{1 - i\gamma\Omega - i\Lambda + Q}{1 - i\gamma\Lambda}\right) \quad \text{and} \quad k_p^2 = \frac{i}{2\Omega}\left(\frac{1 - i\gamma\Omega - i\Lambda - Q}{1 - i\gamma\Lambda}\right), \tag{37}$$

and set

$$m_t = \frac{\gamma}{\gamma - 1}\left(1 + i\Omega k_t^2\right) \quad \text{and} \quad m_p = \frac{\gamma}{\gamma - 1}\left(1 + i\Omega k_p^2\right). \tag{38}$$

We note that Equation (37) also holds for plane and spherical harmonic waves [6,29]. The constants k_p and k_t correspond to acoustic and thermal modes, respectively [29]. The acoustic mode has a small imaginary part and attenuates slowly whereas the thermal mode has both a large real and large imaginary part and attenuates rapidly. Because J_0 and $H_0^{(1)}$ are a numerically satisfactory pair of cylinder functions in the upper half of the complex plane [32, 10.2(iii)], we use them to obtain the fundamental set of solutions to the homogeneous equations (29) and (30):

$$\begin{bmatrix} T(r) \\ P(r) \end{bmatrix} \in \left\{ \begin{bmatrix} J_0(k_p r) \\ m_p J_0(k_p r) \end{bmatrix}, \begin{bmatrix} H_0^{(1)}(k_p r) \\ m_p H_0^{(1)}(k_p r) \end{bmatrix}, \begin{bmatrix} J_0(k_t r) \\ m_t J_0(k_t r) \end{bmatrix}, \begin{bmatrix} H_0^{(1)}(k_t r) \\ m_t H_0^{(1)}(k_t r) \end{bmatrix} \right\}. \tag{39}$$

3.2 Solution of the Inhomogeneous Equations.

Having found a fundamental set of solutions (39) to the homogeneous version of Equations (29) and (30), we now solve the inhomogeneous equations (29) and (30). Introducing new variables for T' and P', we can rewrite the two second order equations (29) and (30) as the first order system

$$\mathbf{u}'(r) = \mathcal{M}(r)\,\mathbf{u}(r) + \mathbf{g}(r), \tag{40}$$

where

$$\mathbf{u}(r) = \begin{bmatrix} T(r) \\ T'(r) \\ P(r) \\ P'(r) \end{bmatrix} \quad \mathcal{M}(r) = \begin{bmatrix} 0 & 1 & 0 & 0 \\ -\frac{i}{\Omega} & -\frac{1}{r} & \frac{i(\gamma-1)}{\gamma\Omega} & 0 \\ 0 & 0 & 0 & 1 \\ \frac{\gamma\left(1-\frac{\Lambda}{\Omega}\right)}{1-i\gamma\Lambda} & 0 & \frac{\gamma\left(1-\frac{\Lambda}{\Omega}\right)+\frac{\Lambda}{\Omega}}{1-i\gamma\Lambda} & -\frac{1}{r} \end{bmatrix} \quad \mathbf{g}(r) = \begin{bmatrix} 0 \\ \frac{1}{\Omega}S(r) \\ 0 \\ -\frac{i\gamma\Lambda}{\Omega(1-i\gamma\Lambda)}S(r) \end{bmatrix}. \tag{41}$$

Using the method of variation of parameters [4], the solution of the inhomogeneous system (40) can be written as

$$\mathbf{u}(r) = \Psi(r)\left(\mathbf{b} + \int_0^r \Psi^{-1}(s)\,\mathbf{g}(s)\,ds\right), \tag{42}$$

where $\mathbf{b}$ is a constant of integration and Ψ is the fundamental matrix

$$\Psi(r) = \begin{bmatrix} J_0(k_p r) & H_0^{(1)}(k_p r) & J_0(k_t r) & H_0^{(1)}(k_t r) \\ -k_p J_1(k_p r) & -k_p H_1^{(1)}(k_p r) & -k_t J_1(k_t r) & -k_t H_1^{(1)}(k_t r) \\ m_p J_0(k_p r) & m_p H_0^{(1)}(k_p r) & m_t J_0(k_t r) & m_t H_0^{(1)}(k_t r) \\ -k_p m_p J_1(k_p r) & -k_p m_p H_1^{(1)}(k_p r) & -k_t m_t J_1(k_t r) & -k_t m_t H_1^{(1)}(k_t r) \end{bmatrix}. \tag{43}$$

We use the Schur complement [26] to calculate Ψ^{-1}. Specifically, we employ the blocking

$$\Psi = \begin{bmatrix} \mathcal{A} & \mathcal{B} \\ \mathcal{C} & \mathcal{D} \end{bmatrix}, \tag{44}$$

where

$$\mathcal{A} = \begin{bmatrix} J_0(k_p r) & H_0^{(1)}(k_p r) \\ -k_p J_1(k_p r) & -k_p H_1^{(1)}(k_p r) \end{bmatrix}, \qquad \mathcal{B} = \begin{bmatrix} J_0(k_t r) & H_0^{(1)}(k_t r) \\ -k_t J_1(k_t r) & -k_t H_1^{(1)}(k_t r) \end{bmatrix}, \tag{45}$$

and

$$\mathcal{C} = m_p A \qquad \text{and} \qquad \mathcal{D} = m_t B. \tag{46}$$

Then

$$\Psi^{-1}=\begin{bmatrix}\mathcal{A} & \mathcal{B}\\ \mathcal{C} & \mathcal{D}\end{bmatrix}^{-1}=\begin{bmatrix}\mathcal{S}^{-1} & -\mathcal{S}^{-1}\mathcal{B}\mathcal{D}^{-1}\\ -\mathcal{D}^{-1}\mathcal{C}\mathcal{S}^{-1} & \mathcal{D}^{-1}+\mathcal{D}^{-1}\mathcal{C}\mathcal{S}^{-1}\mathcal{B}\mathcal{D}^{-1}\end{bmatrix}, \tag{47}$$

where

$$\mathcal{S}=\mathcal{A}-\mathcal{B}\mathcal{D}^{-1}\mathcal{C}. \tag{48}$$

Substituting $\mathcal{D}^{-1}=\frac{1}{m_t}\mathcal{B}^{-1}$ and Equations (46) into Equation (48) yields

$$\mathcal{S}=\frac{m_t-m_p}{m_t}\mathcal{A}. \tag{49}$$

Therefore

$$\Psi^{-1}=\frac{1}{m_t-m_p}\begin{bmatrix}m_t\mathcal{A}^{-1} & -\mathcal{A}^{-1}\\ -m_p\mathcal{B}^{-1} & \mathcal{B}^{-1}\end{bmatrix}, \tag{50}$$

where

$$\mathcal{A}^{-1}(r)=\frac{\pi r}{2i}\begin{bmatrix}-k_pH_1^{(1)}(k_pr) & -H_0^{(1)}(k_pr)\\ k_pJ_1(k_pr) & J_0(k_pr)\end{bmatrix}\quad,\quad \mathcal{B}^{-1}(r)=\frac{\pi r}{2i}\begin{bmatrix}-k_tH_1^{(1)}(k_tr) & -H_0^{(1)}(k_tr)\\ k_tJ_1(k_tr) & J_0(k_tr)\end{bmatrix}.$$

To calculate $\mathcal{A}^{-1}$ and $\mathcal{B}^{-1}$ we used the property that $\mathcal{W}\left(J_0(z),H_0^{(1)}(z)\right)=2i/(\pi z)$ where $\mathcal{W}$ denotes the Wronskian [32]. Thus the inverse of the fundamental matrix is given by

$$\Psi^{-1}(r)=\frac{\pi r}{2i(m_t-m_p)}\begin{bmatrix}-k_pm_tH_1^{(1)}(k_pr) & -m_tH_0^{(1)}(k_pr) & k_pH_1^{(1)}(k_pr) & H_0^{(1)}(k_pr)\\ k_pm_tJ_1(k_pr) & m_tJ_0(k_pr) & -k_pJ_1(k_pr) & -J_0(k_pr)\\ k_tm_pH_1^{(1)}(k_tr) & m_pH_0^{(1)}(k_tr) & -k_tH_1^{(1)}(k_tr) & -H_0^{(1)}(k_tr)\\ -k_tm_pJ_1(k_tr) & -m_pJ_0(k_tr) & k_tJ_1(k_tr) & J_0(k_tr)\end{bmatrix}. \tag{51}$$

Applying the variation of parameters formula (42) we conclude that the general solution of the first order system (40) is

$$\mathbf{u}(r)=\Psi(r)\left(\mathbf{b}+\mathbf{c}(r)\right). \tag{52}$$

Here, $\mathbf{b}=[b_1,b_2,b_3,b_4]^{\mathsf{T}}$ is a vector of unknown constants and $\mathbf{c}(r)=[c_1(r),c_2(r),c_3(r),c_4(r)]^{\mathsf{T}}$ where

$$c_1(r)=\frac{\pi}{2i(m_t-m_p)}\left(E-\frac{m_t}{\Omega}\right)\int_0^r sH_0^{(1)}(k_ps)S(s)\,ds, \tag{53}$$

$$c_2(r)=-\frac{\pi}{2i(m_t-m_p)}\left(E-\frac{m_t}{\Omega}\right)\int_0^r sJ_0(k_ps)S(s)\,ds, \tag{54}$$

$$c_3(r)=-\frac{\pi}{2i(m_t-m_p)}\left(E-\frac{m_p}{\Omega}\right)\int_0^r sH_0^{(1)}(k_ts)S(s)\,ds, \tag{55}$$

$$c_4(r)=\frac{\pi}{2i(m_t-m_p)}\left(E-\frac{m_p}{\Omega}\right)\int_0^r sJ_0(k_ts)S(s)\,ds, \tag{56}$$

and $E=-i\gamma\Lambda/(\Omega(1-i\gamma\Lambda))$. From the first and third rows of Equation (52), we conclude that the general solution of the inhomogeneous system (29) and (30) is given by

$$\begin{aligned}T(r)=&\left(b_1+c_1(r)\right)J_0(k_pr)+\left(b_2+c_2(r)\right)H_0^{(1)}(k_pr)+\\&\left(b_3+c_3(r)\right)J_0(k_tr)+\left(b_4+c_4(r)\right)H_0^{(1)}(k_tr),\end{aligned} \tag{57}$$

$$\begin{aligned}P(r)=&\left(b_1+c_1(r)\right)m_pJ_0(k_pr)+\left(b_2+c_2(r)\right)m_pH_0^{(1)}(k_pr)+\\&\left(b_3+c_3(r)\right)m_tJ_0(k_tr)+\left(b_4+c_4(r)\right)m_tH_0^{(1)}(k_tr).\end{aligned} \tag{58}$$

To determine the constants b_1, b_2, b_3, and b_4 in Equations (57) and (58), as well as the constants d_1 and d_2 in Equation (17), we use boundary conditions (18)–(23). To apply the first condition (18), we consider $\lim_{r\to 0}T(r)$ in Equation (57). By using the approximation $H_0^{(1)}(r)\approx(2i/\pi)\ln(r)$

[32], which is valid for small r, along with repeated application of L'Hopital's Rule, we conclude that condition (18) gives

$$b_2 + b_4 = 0. \tag{59}$$

Similarly, by considering $\lim_{r\to 0} P(r)$, we conclude that condition (19) gives

$$b_2 m_p + b_4 m_t = 0. \tag{60}$$

Therefore, since $m_p \neq m_t$, Equations (59) and (60) imply

$$b_2 = b_4 = 0. \tag{61}$$

Thus the coupled solution given in Equation (57) and (58) simplifies to

$$\begin{aligned} T(r) = &\left(b_1 + c_1(r)\right) J_0(k_p r) + c_2(r) H_0^{(1)}(k_p r) + \\ &\left(b_3 + c_3(r)\right) J_0(k_t r) + c_4(r) H_0^{(1)}(k_t r), \end{aligned} \tag{62}$$

$$\begin{aligned} P(r) = &\left(b_1 + c_1(r)\right) m_p J_0(k_p r) + c_2(r) m_p H_0^{(1)}(k_p r) + \\ &\left(b_3 + c_3(r)\right) m_t J_0(k_t r) + c_4(r) m_t H_0^{(1)}(k_t r). \end{aligned} \tag{63}$$

Using Equations (62) and (63) and the four boundary conditions (20)–(23), we obtain the linear system of four equations in four unknown constants b_1, b_3, d_1, and d_2 given by

$$\begin{bmatrix} J_0(k_p R) & J_0(k_t R) & -J_0(kR) & -H_0^{(1)}(kR) \\ k_p J_1(k_p R) & k_t J_1(k_t R) & -\frac{K_S}{K_F} k J_1(kR) & -\frac{K_S}{K_F} k H_1^{(1)}(kR) \\ m_p k_p J_1(k_p R) & m_t k_t J_1(k_t R) & 0 & 0 \\ 0 & 0 & J_0(kR_S) & H_0^{(1)}(kR_S) \end{bmatrix} \begin{bmatrix} b_1 \\ b_3 \\ d_1 \\ d_2 \end{bmatrix} = \begin{bmatrix} F_1 \\ F_2 \\ F_3 \\ 0 \end{bmatrix}, \tag{64}$$

where

$$F_1 = -c_1(R) J_0(k_p R) - c_2(R) H_0^{(1)}(k_p R) - c_3(R) J_0(k_t R) - c_4(R) H_0^{(1)}(k_t R), \tag{65}$$

$$F_2 = -k_p c_1(R) J_1(k_p R) - k_p c_2(R) H_1^{(1)}(k_p R) - k_t c_3(R) J_1(k_t R) - k_t c_4(R) H_1^{(1)}(k_t R), \tag{66}$$

$$\begin{aligned} F_3 = &-m_p k_p c_1(R) J_1(k_p R) - m_p k_p c_2(R) H_1^{(1)}(k_p R) - \\ &m_t k_t c_3(R) J_1(k_t R) - m_t k_t c_4(R) H_1^{(1)}(k_t R). \end{aligned} \tag{67}$$

Solving the third row for b_3 and the fourth row for d_2 and then substituting these expressions into the two other rows we can reduce the system (64) to the 2×2 system

$$\begin{bmatrix} J_0(k_p R) - \frac{m_p k_p J_1(k_p R) J_0(k_t R)}{m_t k_t J_1(k_t R)} & \frac{J_0(kR_S) H_0^{(1)}(kR)}{H_0^{(1)}(kR_S)} - J_0(kR) \\ k_p J_1(k_p R)\left(1 - \frac{m_p}{m_t}\right) & \frac{K_S k}{K_F}\left(\frac{J_0(kR_S) H_1^{(1)}(kR)}{H_0^{(1)}(kR_S)} - J_1(kR)\right) \end{bmatrix} \begin{bmatrix} b_1 \\ d_1 \end{bmatrix} = \begin{bmatrix} F_1 - \frac{J_0(k_t R) F_3}{m_t k_t J_1(k_t R)} \\ F_2 - \frac{F_3}{m_t} \end{bmatrix}. \tag{68}$$

The 2×2 system (68) can now be solved for b_1 and d_1, and using those values in the 4×4 system (64), we can find b_3 and d_2. We now have a complete solution to the coupled temperature and pressure system given by Equations (62) and (63). At this point, we remind the reader that all quantities in these equations are nondimensional, but that they can be converted back to physical units using Equation (24).

4 Finite-Element Computation of the Solution.

As an additional check, we compared the analytical solution derived in the previous section to a finite element solution computed on the two-dimensional domain shown in Figure 2. Our finite element implementation, which was developed using the FEniCS package [24], is a first step towards a computational model for QEPAS and ROTADE sensors in three dimensions with realistic geometry. One of our major motivations for deriving the cylindrically symmetric analytical solution is that it can be used to help verify the correctness of such a computational model.

For the finite-element results in this paper, we solved the coupled Helmholtz system consisting of the the Morse-Ingard equations (13) and (14) in a disk-shaped fluid domain, Ω_{fluid}, and the heat equation (15) in an annular solid domain, Ω_{solid}, with boundary and interfacial conditions given by Equations (20)–(23). Since FEniCS does not support complex arithmetic, we decomposed the variables into real and imaginary components, $T = T_1 + iT_2$ and $P = P_1 + iP_2$, as in [5]. With this decomposition, the entries of the complex-valued finite-element matrices are converted into 2×2 blocks of corresponding real-valued matrices. The mesh was generated using the Gmsh package [14]. The mesh was refined around the source and near the interface between the fluid and solid subdomains (see Figure 3). For our FEniCS implementation, we used linear Lagrange interpolating polynomials on triangular elements. Finally, the assembled system was solved using the sparse LU decomposition algorithm in the PETSc package [1]. The finite element system we solved had approximately 2×10^5 unknowns on a mesh with 10^5 triangular elements. In Figure 3 we show a slightly coarser mesh (with 10^4 triangular elements) which has the same characteristics as our simulation mesh. We note that with a finer mesh it is harder to discern the refinement around the source and at the fluid-solid interface due to the density of the elements. For comparison with the analytical solution, we used linear interpolation to compute the values of the temperature and pressure along the x-axis of the two-dimensional domain.

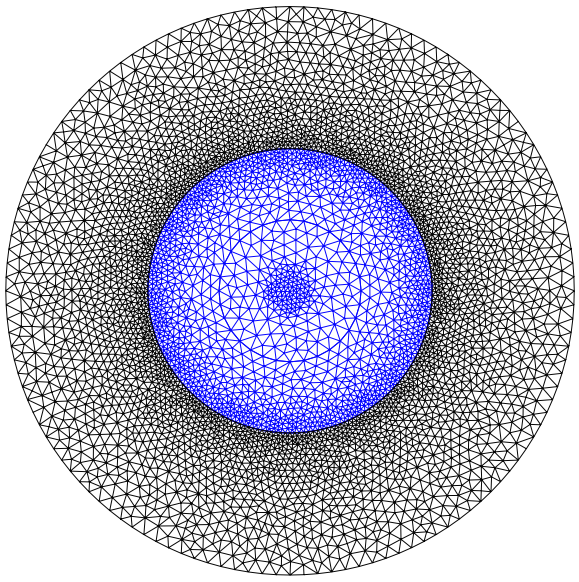

Fig. 3 A finite-element mesh with 10^4 triangular elements for the domain shown in Figure 2.

5 Numerical Results.

In this section, we numerically investigate the solution of the Morse-Ingard equations derived in Section 3. We first verify the correctness of the analytic solution for temperature and pressure by comparison to a purely numerical solution computed via the finite element method. Next, we show that the temperature solution from the Morse-Ingard equations differs significantly

from the solution obtained using the heat equation in the fluid. In particular, we show that the Morse-Ingard solution produces a thermal boundary layer which is not present in the solution obtained using the heat equation in the fluid. This boundary layer results from the interaction of a thermal part and an acoustic part of the solution of nearly equal magnitudes.

For all the numerical simulations, we assume that the fluid is nitrogen gas at a temperature of 300 K and a pressure of 1 bar [36]. The parameter values we used are shown in Table 5. All the parameter values in the simulations closely correspond to those used in our previous modeling of laboratory experiments of QEPAS and ROTADE sensors [35,36]. In the first set of numerical simulations, we assume that the width of the Gaussian source σ is 0.02 mm. In Figure 4 we show the amplitude of the temperature variation in the fluid as a function of the radial distance, r, from the center of the laser beam over the interval $[0, 0.1]$ mm. The three curves show the solution to the heat equation in the fluid (dots), the analytic solution of the Morse-Ingard equations (circles), and the solution of the Morse-Ingard equations via the finite-element method (dashes). The analytic solution of the Morse-Ingard equations agrees with the finite-element solution, thus verifying the accuracy of both solution methods. Also, in Figure 4, we see the amplitudes of the temperature variation given by the Morse-Ingard equations and the heat equation in the fluid agree well for $r \in [0, 0.025]$ mm. However, as r increases, the two amplitudes diverge, as is seen more clearly in Figure 5, which shows the same solutions as Figure 4 over the interval $[0.05, 0.1]$ mm rather than over the full interval $[0, 0.1]$ mm. The solutions of the heat equation and the Morse-Ingard equations disagree in this region. For example, at $r = 0.08$ mm, we see that the amplitude of the temperature given by the Morse-Ingard equations $\left(\approx 3.3 \times 10^{-5} \text{ K}\right)$ is about four times the amplitude of the temperature given by the heat equation $\left(\approx 7.7 \times 10^{-6} \text{ K}\right)$.

Source Frequency	$f = 3.28 \times 10^4$ Hz
Source Width	$\sigma = 2 \times 10^{-5}$ m or 1×10^{-6} m
Radius of Nitrogen Gas Domain	$R = 1 \times 10^{-4}$ m
Outer Radius of Solid Annulus	$R_S = 2 \times 10^{-4}$ m
Thermal Conductivity of Nitrogen Gas	$K_F = 0.0259$ W m^{-1} K^{-1}
Density of Nitrogen Gas	$\rho_0 = 1.123$ kg m^{-3}
Specific Isobaric Heat Capacity of Nitrogen Gas	$C_p = 1041$ J kg^{-1} K^{-1}
Ratio of Specific Heats of Nitrogen Gas	$\gamma = 1.4$
Thermal Expansion of Nitrogen Gas	$\beta = 3.33 \times 10^{-3}$ K^{-1}
Bulk (Volume) Viscosity of Nitrogen Gas	$\eta = 1.3 \times 10^{-5}$ kg m^{-1} s^{-1}
Viscosity of Nitrogen Gas	$\mu = 1.76 \times 10^{-5}$ kg m^{-1} s^{-1}
Speed of Sound in Nitrogen Gas	$c = 353$ m s^{-1}
Thermal Conductivity of Solid	$K_S = 16$ W m^{-1} K^{-1}
Thermal Diffusivity of Solid	$D_S = 4 \times 10^{-6}$ m^2 s^{-1}
Effective Absorption Coefficient	$\alpha_{\text{eff}} = 0.05$ m^{-1}
Laser Power	$W_L = 3 \times 10^{-2}$ W
Thermal Characteristic Length	$l_h = 6.276 \times 10^{-8}$ m
Viscous Characteristic Length	$l_v = 9.199 \times 10^{-8}$ m
—	$\alpha = \frac{\rho_0 \beta c^2}{\gamma} = 333.18$ kg m^{-1} K^{-1} s^{-2}

Table 1 Parameters used in the numerical simulations.

In Figure 6 we plot the phase of the temperature variation relative to the source as a function of r over the interval $[0, 0.1]$ mm. (We assume that the phase of the source is zero, see Equation (11).) Once again, we observe excellent agreement between the analytical and numerical solutions of the Morse-Ingard equations. However, although the phase of the temperature solutions of the Morse-Ingard equations and of the heat equation in the fluid agree well for small r, they differ significantly as r increases.

The pressure solution of the Morse-Ingard equations is dominated by the acoustic mode, which attenuates very slowly, and is therefore nearly constant over the interval $[0, 0.1]$ mm. While we do not include plots of the amplitude or phase of the pressure variation in this paper,

the analytic solution to the Morse-Ingard equations again agrees with the finite-element solution. Both solutions have an amplitude of approximately 0.048 Pa, and they differ from one another by less than one percent. Similarly, the phase of the pressure solution is nearly constant with an approximate value of 1.59 radians.

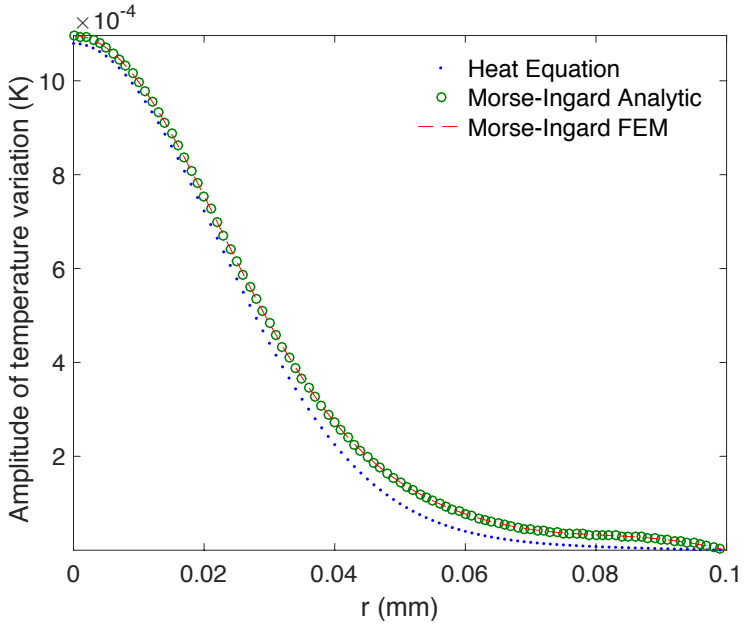

Fig. 4 Amplitude of temperature versus radial distance from the center of the laser beam. The width of the Gaussian beam is $\sigma = 0.02$ mm. The figure shows the solution in the fluid only.

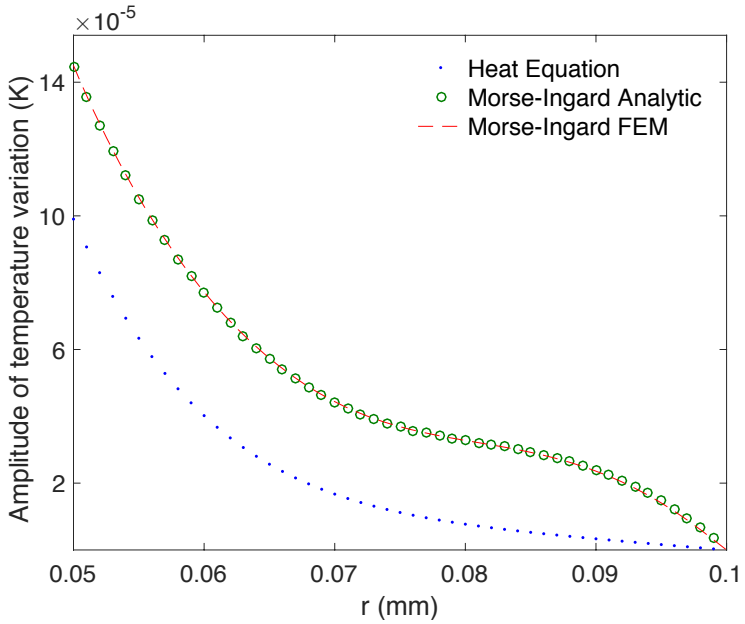

Fig. 5 Amplitude of temperature versus radial distance from the center of the laser beam. The width of the Gaussian beam is $\sigma = 0.02$ mm. The figure is a zoomed-in view of the tail of Figure 4.

Having examined the solution in the fluid, we now consider the solution in a larger domain which includes both the fluid and the solid annulus surrounding the fluid. In Figure 7 we plot the amplitude of the temperature variation in the fluid as well as in the solid annulus surrounding the fluid for $r \in [0, 0.2]$ mm on a log scale for both the Morse-Ingard equations and the heat

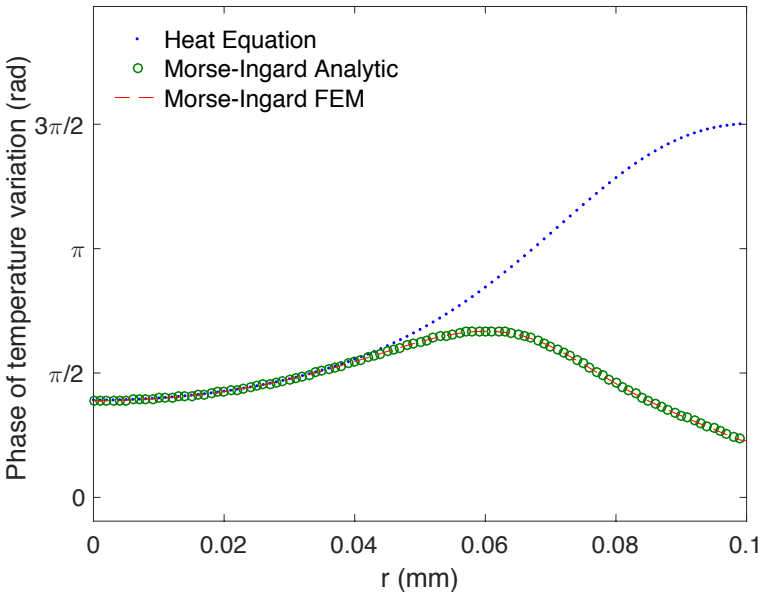

Fig. 6 Phase of temperature versus radial distance from the center of the laser beam. The width of the Gaussian beam is $\sigma = 0.02$ mm. The figure shows the solution in the fluid only.

equation in the fluid. The width of the laser source is still $\sigma = 0.02$ mm, and the fluid-structure interface is located at $r = 0.1$ mm. At the interface, the temperature solution to the Morse-Ingard equations is between one and two orders of magnitude larger than the solution obtained using the heat equation in the fluid. Since the amplitude of vibration of the quartz tuning fork in a ROTADE sensor is primarily determined by the temperature variation at the fluid-structure interface [36], this result strongly indicates that the solution of the heat equation in the fluid is likely to be a poor approximation when modeling thermal effects in trace gas sensors. In particular, since the signal-to-noise ratio in a tuning fork sensor is approximately 1000, (*i.e.*, 30 dB) [11], ROTADE sensors can readily distinguish between temperature variations that are less than an order of magnitude apart.

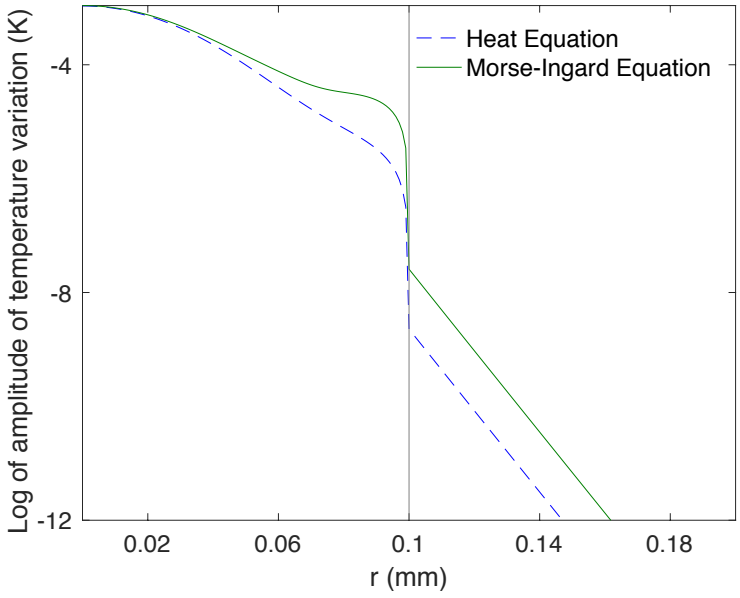

Fig. 7 Semilog plot of the amplitude of the temperature variation as a function of radial distance from the center of the laser beam. The width of the Gaussian beam is $\sigma = 0.02$ mm. The figure shows the solution in both the fluid, $r \in [0, 0.1]$ mm, and the surrounding solid, $r \in [0.1, 0.2]$ mm.

In the second set of numerical simulations, we assume a narrower width for the Gaussian source, *i.e.*, $\sigma = 0.001$ mm. In Figure 8, we show the amplitude of the temperature variation in the fluid as a function of the radial distance, r, from the center of the laser beam over the interval $[0, 0.1]$ mm. The two curves show the solution obtained using the heat equation in the fluid and the analytic solution of the Morse-Ingard equations. Because the source is narrower, in this case, the solution decays much faster than in the previous case, as can be seen by comparing Figures 4 and 8. In addition, we observe a boundary layer, as shown in Figure 9. This figure shows the same solutions as Figure 8 but over the smaller interval $[0.05, 0.1]$ mm. While the solution to the heat equation decreases monotonically, the solution to the Morse-Ingard equation increases for $r \in [0.06, 0.08]$ mm before decreasing for $r \in [0.08, 0.1]$ mm. According to Morse and Ingard, for a plane harmonic wave, the width of the temperature boundary layer is $\sqrt{2l_h c/\omega} \approx 0.0147$ mm [29, p. 286]. In Figure 9, we see that for the cylindrical harmonic wave, the width of the boundary layer is approximately 0.05 mm, which is on the same order of magnitude as that predicted by Morse and Ingard.

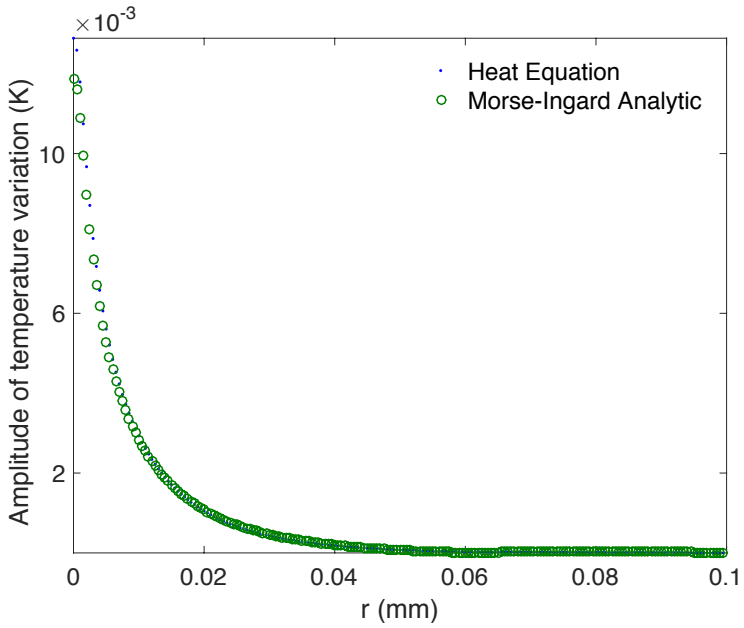

Fig. 8 Amplitude of the temperature variation as a function of radial distance from the center of the laser beam. The width of the Gaussian beam is narrower than in Figures 4–7 with $\sigma = 0.001$ mm. The figure shows the solution in the fluid only.

In Figure 10, we show the phase of the temperature variation as a function of r over the interval $[0, 0.1]$ mm. Comparing Figures 6 and 10, we also see that there is a more rapid change in phase of the temperature solution of the Morse-Ingard equations when the Gaussian beam is narrower.

Both the thermal wave, T, and the pressure wave, P, contain a thermal part and an acoustic part. The acoustic part of the temperature solution is given by the first two terms of Equation (62), *i.e.*, $(b_1 + c_1(r)) J_0(k_p r) + c_2(r) H_0^{(1)}(k_p r)$, and the thermal part of the temperature solution is given by the last two terms of Equation (62), *i.e.*, $(b_3 + c_3(r)) J_0(k_t r) + c_4(r) H_0^{(1)}(k_t r)$. The acoustic and thermal parts of the pressure solution are given by the analogous terms of Equation (63). In Figure 11 we show the acoustic and thermal parts of the temperature variation using the source with the narrower width of $\sigma = 0.001$ mm. For small r, the thermal part of the solution is about two orders of magnitude larger than the acoustic part. For example, at $r = 0.02$ mm, the amplitude of the thermal part of the temperature solution (≈ 0.001 K) is about 24 times the amplitude of the acoustic part of the temperature solution $\left(\approx 4.17 \times 10^{-5} \text{ K}\right)$. As r increases, the acoustic part remains relatively constant while the thermal part decreases. When both parts are roughly the same order of magnitude, they produce the variation in amplitude in the radial direction seen in Figure 9. In Figure 12, we show the acoustic and thermal parts of the pressure variation. The acoustic part of the solution

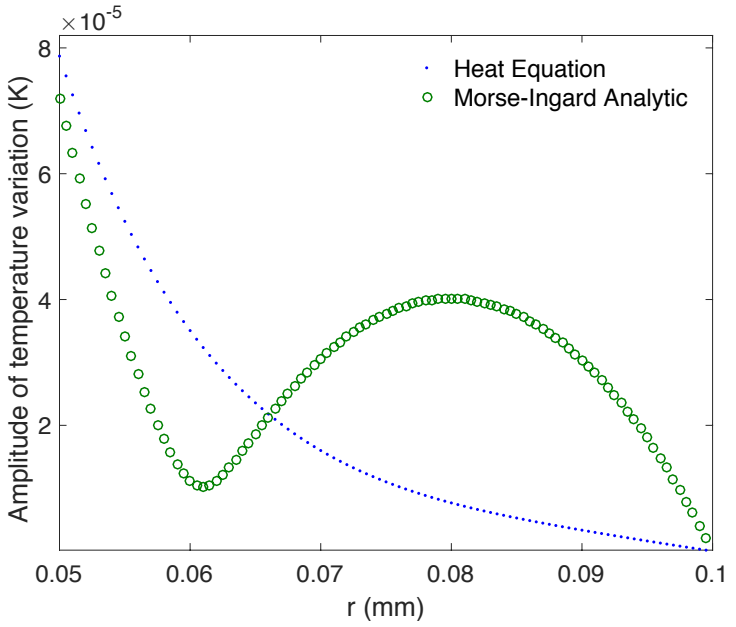

Fig. 9 Amplitude of the temperature variation as a function of radial distance from the center of the laser beam. The figure is a zoomed-in view of the tail of Figure 8. The width of the Gaussian beam is $\sigma = 0.001$ mm.

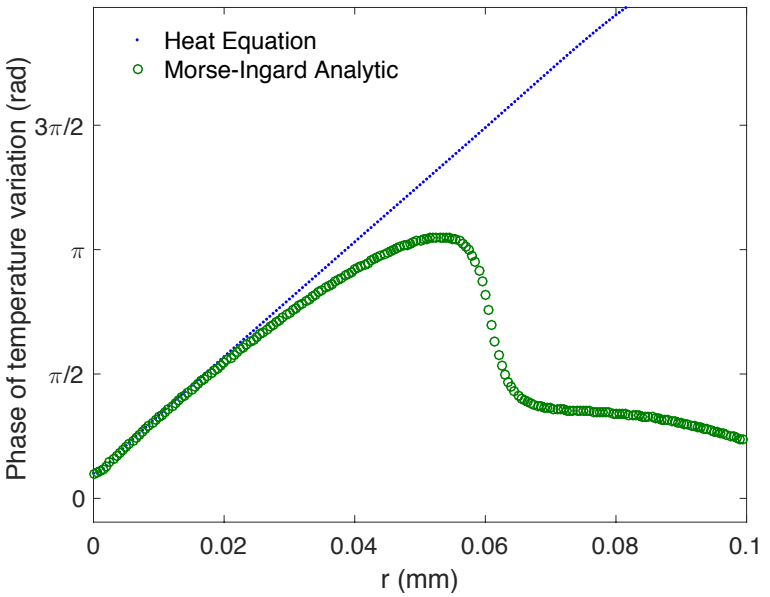

Fig. 10 Phase of the temperature variation as a function of radial distance from the center of the laser beam. The width of the Gaussian beam is the same as in Figures 8 and 9 with $\sigma = 0.001$ mm. The figure shows the solution in the fluid only.

is at least two orders of magnitude larger than the thermal part of the solution. For example, at $r = 0.02$ mm, the amplitude of the acoustic part of the pressure solution (≈ 0.0486 Pa) is about 5900 times the amplitude of the thermal part of the pressure solution $\left(\approx 8.27 \times 10^{-6} \text{ Pa}\right)$. As r increases, the ratio of the amplitude of the acoustic part to the thermal part of the pressure solution also increases. In summary, the thermal mode dominates the temperature solution away from the boundary layer, while the acoustic mode dominates the pressure solution over the entire fluid domain. For both the temperature and pressures solutions, the thermal mode attenuates rapidly as described by Morse and Ingard [29, p. 282-283].

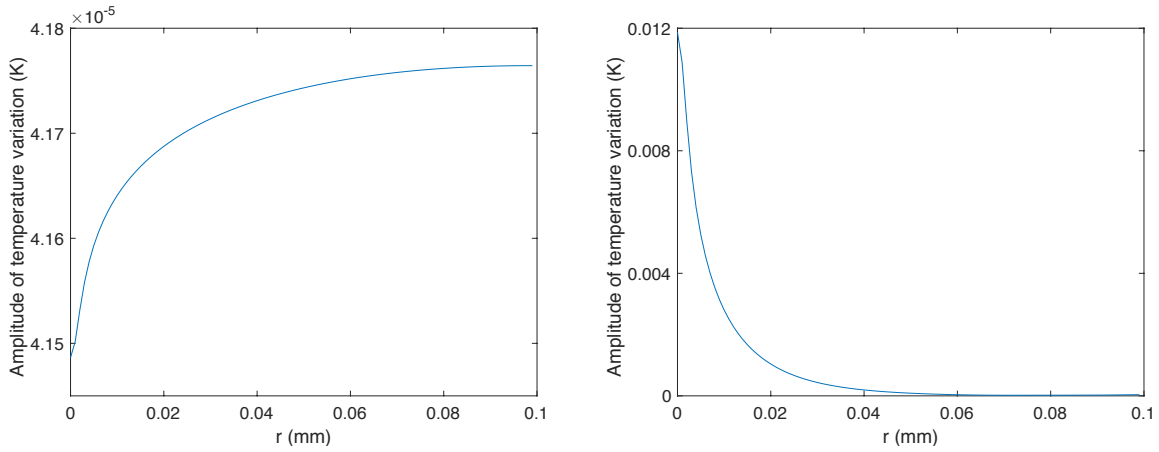

(a) Acoustic part of temperature. (b) Thermal part of temperature.

Fig. 11 Amplitude of (a) the acoustic part and (b) the thermal part of temperature variation as a function of radial distance from the center of the laser beam. The width of the Gaussian beam is $\sigma = 0.001$ mm. The figures show the solution in the fluid only.

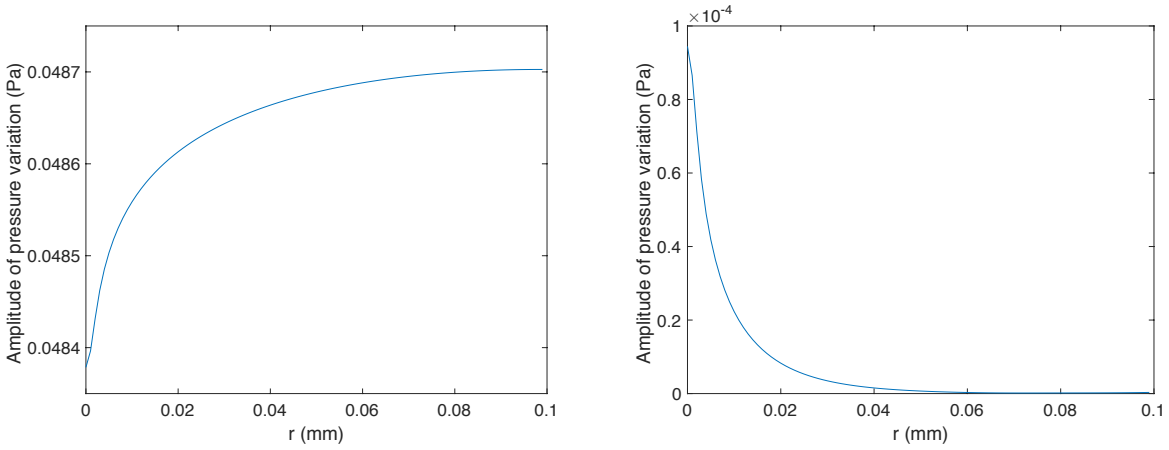

(a) Acoustic part of pressure. (b) Thermal part of pressure.

Fig. 12 Amplitude of (a) the acoustic part and (b) the thermal part of pressure variation as a function of radial distance from the center of the laser beam. The width of the Gaussian beam is $\sigma = 0.001$ mm. The figures show the solution in the fluid only.

6 Conclusions.

We derived an analytic solution to the coupled system of pressure-temperature equations of Morse and Ingard. By assuming that the laser source can be represented as a time-harmonic function and by using the cylindrical symmetry of the domain, we converted the partial differential equations into ordinary differential equations for which the independent variable is given by the radial distance from the center of the laser beam. We solved these ordinary differential equations using the method of variation of parameters. The constants of integration were found by solving a system of linear equations obtained from the boundary conditions. We then verified the correctness of the analytic solution by comparing it to the solution computed via the finite-element method. We also compared the solution of the Morse-Ingard equations to the solution of the heat equation in the fluid and found that the coupled nature of the Morse-Ingard equations results in a significantly larger temperature variation than that predicted by the heat equation, especially in the solid near the fluid-solid interface. This discrepancy demonstrates the importance of using the Morse-Ingard equations for more realistic computational modeling of trace gas sensors.

In addition, because the Morse-Ingard equations include parameters that model viscothermal effects, the analytic solution we derived in this paper provides a starting point for the

development of a mathematical model of QEPAS and ROTADE sensors which accounts for the damping of the tuning fork. The ultimate goal of such an improved model is to allow for the efficient optimization of the tuning fork geometry via computer simulations so that the full benefit of this promising technology may be realized.

An important application of the analytical solution we derived is that it can be used to verify the correctness of computational models for trace gas sensors that are based on finite-element solutions of the Morse-Ingard equations. In particular, because we correctly model the source, we expect the behavior of the cylindrically symmetric pressure and temperature solutions to be qualitatively similar to that in a trace gas sensor. By comparison, the plane wave solutions we used in past verification studies are qualitatively very different [5].

To quantify the performance of a QEPAS/ROTADE sensor, the Morse-Ingard equations in the fluid need to be coupled to the system of equations for the displacement of the tuning fork. As we will show in future work, this coupling is via conditions on the interface between the fluid and tuning fork. In particular, the condition on the tuning fork due to the fluid includes a term that involves the viscous stress tensor of the fluid and models the damping of the tuning fork due to its motion through the viscous fluid [16]. With the recent interest in further miniaturizing these devices, the thermal and viscous boundary layers become more significant, emphasizing the importance of our new model [15].

References

1. Balay, S., Abhyankar, S., Adams, M.F., Brown, J., Brune, P., Buschelman, K., Dalcin, L., Eijkhout, V., Gropp, W., Kaushik, D., Knepley, M., McInnes, L., Rupp, K., Smith, B., Zampini, S., Zhang, H.: PETSc Webpage. http://www.mcs.anl.gov/petsc (2015)
2. Bell, A.: On the production and reproduction of sound by light. Am. J. Sci. **20**, 305–324 (1880)
3. Bossart, R., Joly, N., Bruneau, M.: Hybrid numerical and analytical solutions for acoustic boundary problems in thermo-viscous fluids. J. Sound Vib. **263**, 69–84 (2003)
4. Boyce, W., DiPrima, R.: Elementary Differential Equations, 8th edn. John Wiley (2005)
5. Brennan, B., Kirby, R., Zweck, J., Minkoff, S.: High-performance python-based simulations of pressure and temperature waves in a trace gas sensor. Proceedings of PyHPC 2013: Python for High Perfomance and Scientific Computing (2013)
6. Cao, Y., Diebold, G.J.: Effects of heat conduction and viscosity on photoacoustic waves from droplets. Optical Engineering **36**(2), 417–422 (1997)
7. Chorin, A.J., Marsden, J.E.: A Mathematical Introduction to Fluid Mechanics. Springer-Verlag, New York, N.Y. (1979)
8. Cordioli, J., Martins, G., Mareze, P., Jordan, R.: A comparison of models for visco-thermal acoustic problems. In: Inter-Noise. International Institute of Noise Control Engineering (2010)
9. Curl, R., Capasso, F., Gmachl, C., Kosterev, A., McManus, B., Lewicki, R., Pusharsky, M., Wysocki, G., Tittel, F.: Quantum cascade lasers in chemical physics. Chemical Physics Letters **487**, 1–18 (2010)
10. Dong, L., Kosterev, A., Thomazy, D., Tittel, F.: Compact portable QEPAS multi-gas sensor. Proc. of SPIE **7945**, 79,450R:1 – 79,450R:7 (2011)
11. Dong, L., Kosterev, A.A., Thomazy, D., Tittel, F.K.: QEPAS spectrophones: design, optimization, and performance. Appl. Phys. B **100**, 627–635 (2010)
12. Firebaugh, S., Sampaolo, A., Patimisco, P., Spagnolo, V., Tittel, F.: Modeling the dependence of fork geometry on the performance of quartz enhanced photoacoustic spectroscopic sensors. In: Conference on Lasers and Electro-Optics, ATu1J3. San Jose, CA (2015)
13. Firebaugh, S., Terray, E., Dong, L.: Optimization of resonator radial dimensions for quartz enhanced photoacoustic spectroscopy systems. In: Proc. SPIE 8600, Laser Resonators, Microresonators, and Beam Control XV, 86001S (2013)
14. Geuzaine, C., Remacle, J.F.: Gmsh: a three-dimensional finite element mesh generator with built-in pre- and post-processing facilities. International Journal for Numerical Methods in Engineering **79**(11), 1309–1331 (2009)
15. Gliere, A., Rouxel, J., Parvitte, B., Boutami, S., Zeninari, V.: A coupled model for the simulation of miniaturized and integrated photoacoustic gas detector. International Journal of Thermophysics **34**, 2119–2135 (2013)
16. Joly, N., Bruneau, M., Bossart, R.: Coupled equations for particle velocity and temperature variation as the fundamental formulation of linear acoustics in thermo-viscous fluids at rest. Acta Acustica united with Acustica **92**, 202–209 (2006)
17. Kampinga, R.: Viscothermal acoustics using finite elements: Analysis tools for engineers. Ph.D. thesis, University of Twente, Enschede, The Netherlands (2010)
18. Kokubun, K., Hirata, M., Murakami, H., Toda, Y., Ono, M.: A bending and stretching mode crystal oscillator as a friction vacuum gauge. Vacuum **34**, 731–735 (1984)
19. Kosterev, A., Bakhirkin, Y., Curl, R., Tittel, F.: Quartz-enhanced photoacoustic spectroscopy. Optics Letters **27**, 1902–1904 (2002)
20. Kosterev, A., Doty III, J.: Resonant optothermoacoustic detection: technique for measuring weak optical absorption by gases and micro-objects. Optics Letters **35**(21), 3571 – 3573 (2010)
21. Landau, L.D., Lifshitz, E.M.: Fluid Mechanics. Addison-Wesley Publishing Company, Reading, MA (1959)
22. Lavergne, T., Joly, N., Durand, S.: Acoustic thermal boundary condition on thin bodies: Application to membranes and fibres. Acta Acustica united with Acustica **99**, 524–536 (2013)
23. Lewicki, R., Jahjah, M., Ma, Y., Stefanski, P., Tarka, J., Razeghi, M., Tittel, F.: Current Status of Mid-Infrared Semiconductor Laser Based Sensor Technologies for Trace Gas Sensing Applications, chap. 23. SPIE Press (2013). In: M. Razeghi, L. Esaki and K. von Klitzing (Eds.), "The Wonder of Nanotechnology: Present and Future of Optoelectronics Quantum devices and their applications for Environment, Health, Security, and Energy"
24. Logg, A., Mardal, K., Wells, G.: Automated Solution of Differential Equations by the Finite Element Method. Springer (2012)

25. Ma, Y., Lewicki, R., Razeghi, M., Tittel, F.: QEPAS based ppb-level detection of CO and N2O using a high power CW DFB-QCL. Opt. Express **21**(1), 1008–1019 (2013). DOI 10.1364/OE.21.001008
26. Meyer, C.: Matrix Analysis and Applied Linear Algebra. SIAM (2000)
27. Miklos, A., Bozoki, Z., Jiang, Y., Feher, M.: Experimental and theoretical investigation of photoacoustic-signal generation by wavelength-modulated diode lasers. Appl. Phys. B **58**, 483–492 (1994)
28. Miklós, A., Schäfer, S., Hess, P.: Photoacoustic Spectroscopy, Theory. In: J. Lindon, G. Tranter, J. Holmes (eds.) Encyclopedia of Spectroscopy and Spectrometry, pp. 1815–1822. Academic Press, London UK (1999)
29. Morse, P., Ingard, K.: Theoretical Acoustics. Princeton University Press, New Jersey (1986)
30. Newell, W.: Miniaturization of tuning forks. Science (New Series) **161**(3848), 1320 – 1326 (1968)
31. Nye, J.: Physical Properties of Crystals. Oxford University Press, New York (2000)
32. Olver, F., Maximon, L.: Digital Library of Mathematical Functions: Chapter 10 Bessel Functions (2014). http://www.dlmf.nist.gov/10
33. Patimisco, P., Scamarcio, G., Tittel, F., Spagnolo, V.: Quartz-enhanced photoacoustic spectroscopy: A review. Sensors: Special Issue "Gas Sensors-2013" **14**, 6165–6206 (2014)
34. Petra, N., Kosterev, A., Zweck, J., Minkoff, S., Doty III, J.: Numerical and experimental investigation for a resonant optothermoacoustic sensor. In: Conference on Lasers and Electro-Optics, CMJ6. San Jose, CA (2010)
35. Petra, N., Zweck, J., Kosterev, A., Minkoff, S., Thomazy, D.: Theoretical analysis of a quartz-enhanced photoacoustic spectroscopy sensor. Appl Phys B **94**, 673–680 (2009)
36. Petra, N., Zweck, J., Minkoff, S., Kosterev, A., Doty III, J.: Modeling and design optimization of a resonant optothermoacoustic trace gas sensor. SIAM Journal on Applied Mathematics pp. 309–332 (2011)
37. Petra, N., Zweck, J., Minkoff, S., Kosterev, A., Doty III, J.: Validation of a model of a resonant optothermoacoustic trace gas sensor. In: Conference on Lasers and Electro-Optics, JTuI115. Baltimore, MD (2011)
38. Tittel, F., Lewicki, R., Jahjah, M., Foxworth, B., Ma, Y., Dong, L., Griffin, R., Krzempek, K., Stefanski, P., Tarka, J.: Mid-Infrared Laser based Gas Sensor Technologies for Environmental Monitoring, Medical Diagnostics, Industrial and Security Applications, chap. 21. Springer Science+Business Media, Dordrecht (2014). In: M.F. Pereira and O. Shulika (Eds.), "Terahertz and Mid Infrared Radiation: Detection of Explosives and CBRN (Using Terahertz)"
39. Zheng, H., Dong, L., Yin, X., Liu, X., Wu, H., Zhang, L., Ma, W., Yin, W., Jia, S.: Ppb-level QEPAS NO_2 sensor by use of electrical modulation cancellation method with a high power blue LED. Sensors and Actuators B: Chemical **208**, 173–179 (2015)